

# HST FUV OBSERVATIONS OF BRIGHTEST CLUSTER GALAXIES: THE ROLE OF STAR FORMATION IN COOLING FLOWS AND BCG EVOLUTION

KIERAN O'DEA, ALICE C. QUILLEN

Department of Physics and Astronomy, University of Rochester, Rochester, NY 14627, USA

BRADFORD SNIOS, GRANT TREMBLAY, CHRIS P. O'DEA, STEFI A. BAUM, KEVIN CHRISTIANSEN

Department of Physics, Rochester Institute of Technology, 84 Lomb Memorial Drive, Rochester, NY 14623-5603, USA

MEGAN DONAHUE, MARK VOIT

Michigan State University, Physics and Astronomy Dept., East Lansing, MI 48824-2320, USA

& ALASTAIR C. EDGE

Institute for Computational Cosmology, Department of Physics, Durham University, Durham DH1 3LE, Great Britain

LIST AND ORDER TO BE DETERMINED

*Draft version September 28, 2009*

## ABSTRACT

We present Hubble Space Telescope Advanced Camera for Surveys (ACS) far ultraviolet (FUV) images of the Ly $\alpha$  and continuum emission of the luminous emission-line nebulae in 7 galaxies from the Rosat brightest cluster sample chosen based on their elevated H $\alpha$  flux. The emission in both FUV continuum and Ly $\alpha$  is resolved over a region 5-10 kpc large. Both continuum and line emission contains clumps, but the Ly $\alpha$  emission also contains a diffuse or filamentary component. Star formation rates estimated from the FUV continuum are about 10 times lower than those estimated from the infrared, however both the Balmer decrement in the central few arcseconds and detection of CO in most of these galaxies imply that there are regions of high extinction that could have absorbed much of the FUV continuum. Only 2 of the brightest cluster galaxies have resolved extended radio emission as seen with VLA archival observations. The 4 galaxies with archival deep Chandra observations exhibit lopsided X-ray emission. A low feedback state for the AGN could allow increased condensation of the hot gas into the center of the galaxy and feeding the star formation, however this would not account for the lopsided X-ray morphology (if this is significantly different than in other BCGs). Alternately, disturbances in the intergalactic medium (IGM) could be associated with the enhanced star formation.

*Subject headings:*

## 1. INTRODUCTION

Ly $\alpha$  and far-ultraviolet continuum observations provide unique constraints on the physical properties of the nebulae in clusters. The far-UV continuum together with optical and infrared observations constrain the star formation history and the properties of young stars associated with the nebula. The Ly $\alpha$  to H $\alpha$  or H $\beta$  flux ratio is a diagnostic of ionization, metal and dust content (Ferland & Osterbrock 1985; Binette et al. 1993).

Cooling flow clusters exhibit extended Ly $\alpha$  emission (Hu 1992) and far UV continuum emission (O'Dea et al. 2004). The previous study of two brightest cluster galaxies (BCGs), Abell 1795 and Abell 2597 (O'Dea et al. 2004), found that the nebula exhibited both a diffuse component Ly $\alpha$  and more compact features such as knots and filaments. The Ly $\alpha$  emission was closely tied to the radio morphology suggesting that star formation and associated ionization was present at the edges of radio lobes.

In this study we enlarge the sample of objects studied by including more distant BCGs and those with higher star formation rates. Brightest cluster galaxies (BCGs)

with high H $\alpha$  luminosities were chosen from the ROSAT Brightest Cluster Sample (BCS) (Ebeling et al. 1998). Their H $\alpha$  luminosities are in the range  $10^{42}$ – $10^{43}$  erg/s. These galaxies have been observed with the Spitzer Space Telescope (Quillen et al. 2008; O'Dea et al. 2008).

Not all cooling flow BCGs have evidence of recent or ongoing star formation (O'Dea et al. 2008; Loubser et al. 2009). Hence BCGs exhibiting elevated rates of star formation could be those experiencing a low level of feedback from the AGN. Evidence for residual cooling can be inferred from the reservoirs of cold gas found in BCGs. Alternatively star formation could also be attributed to stripping from a gas rich galaxy (Holtzman et al. 1996). Recent estimates of condensation and star formations rates show that in some systems are they are in near agreement (e.g., O'Dea et al. 2008). Recently Rafferty et al. (2008) found that star formation tends to occur when the central cooling time drops below a critical value. In this paper by resolving the region of star formation, over a large sample of BCGs we aim to test some of these possibilities.

## 2. OBSERVATIONS

TABLE 1  
OBSERVATION LOG

Source	RA	Dec	$z$	kpc/''	Line/Cont	Filter
Abell 11	00:12:33.87	-16:28:07.7	0.151	2.60	Line	F125LP
					Cont.	F150LP
Abell 1664	13:03:42.52	-24:14:43.8	0.128	2.26	Line	F125LP
					Cont.	F150LP
Abell 1835	14:01:02.10	+02:52:42.8	0.253	3.91	Line	F140LP
					Cont.	F165LP
RXJ 2129+00	21:29:39.96	+00:05:21.2	0.235	3.70	Line	F140LP
					Cont.	F165LP
ZWCL 348	01:06:49.39	+01:03:22.7	0.254	3.92	Line	F140LP
					Cont.	F165LP
ZWCL 3146	10:23:39.62	+04:11:10.8	0.290	4.32	Line	F140LP
					Cont.	F165LP
ZWCL 8193	17:17:19.21	+42:26:59.9	0.175	2.94	Line	F140LP
					Cont.	F150LP

NOTE. — The exposure time in each long pass filter was 1170s. Positions are given in degrees for epoch J2000 and are measured from radio source positions in archival VLA data at 8.5 or 5 GHz.

TABLE 2  
STAR FORMATION RATES

Galaxy	$M(H_2)$ ( $10^{10} M_\odot \text{ yr}^{-1}$ )	$SFR_{IR}$ ( $M_\odot \text{ yr}^{-1}$ )	$SFR_{H\alpha}$ ( $M_\odot \text{ yr}^{-1}$ )	$SFR_{FUV}$ ( $M_\odot \text{ yr}^{-1}$ )	Balmer Dec $H\alpha/H\beta$
Abell 11	1.1	35	9.7	4.8	...
Abell 1664	1.9	15	5.6	4.6	5.2
Abell 1835	7.9	125	40.5	11.7	5
ZWCL 348		52	15.5	6.1	4.27
ZWCL 3146	7.0	67	47.1	12.4	3.7
ZWCL 8193	1.5	59	7.6	5.4	5.9
RXJ 2129+00		13	2.3	0.9	2

NOTE. — Notes on table: Infrared estimated star formation rates are by O’Dea et al. (2008) except for Abell 1835 and ZWCL 3146 which are by Egami et al. (2006). These star formation rates are estimated from the 8 and 24  $\mu\text{m}$  fluxes (Quillen et al. 2008). Molecular gas mass estimates for Abell 11, Abell 1665, Abell 1835, and ZWCL 3146. by Edge (2001), but corrected to a Hubble constant of  $75 \text{ Mpc}^{-1} \text{ km s}^{-1}$ . The ZWCL 8193 molecular mass is by Salome & Combes (2003). Note ZWCL 3146 also contains about  $10^{10} M_\odot$  of warm molecular hydrogen (Egami et al. 2006). Star formation rates are estimated from the limited-aperture observations by Crawford et al. (1999) (long slit of width  $1''.3$ ) excepting for ZWCL 348 which used the  $H\alpha$  flux from the Sloan Digital Sky Survey archive (and a  $3''$  diameter fiber). Neither the  $H\alpha$  or UV based star formation rate estimates have been corrected for internal extinction.

TABLE 3  
LY $\alpha$  FLUXES

Source	Radius of Aperture ( $''$ )	Flux ( $e^{-1} \text{ s}^{-1}$ ) ( $e^{-1} \text{ s}^{-1}$ )	Ly $\alpha$ Flux ( $10^{-14} \text{ erg cm}^{-2} \text{ s}^{-1}$ )
Abell 11	2	6.5	7
Abell 1664	3	3.6	8
Abell 1835	2	3.8	14
ZWCL 348	2	2.1	10
ZWCL 3146	3	1.7	15
ZWCL 8193	2	15.9	6
RXJ 2129+00	2	0.3	2

NOTE. — Fluxes were measured using aperture photometry and an aperture that covers the bulk of the emission visible in Figures 1-7

### 2.1. FUV images

Observations were obtained with the Solar Blind Channel (SBC) MAMA detector of the Advanced Camera for Surveys (ACS) (Clampin et al. 2004) on the Hubble Space Telescope (HST). Each galaxy was observed in two long pass filters, the one containing the Ly $\alpha$  line, the other redward of this line to measure the continuum. The F140LP filter containing the Ly $\alpha$  line was used for all galaxies except the nearer BCGs, Abell 11 and Abell 1664, which were observed using the F125LP filter. The continuum filter chosen was F150LP for objects with redshift  $0.11 < z < 0.19$  (ZWCL8193, Abell 11, and Abell 1664) and the F165LP filter for the remaining objects with  $0.19 < z < 0.31$  (Abell 1835, ZWCL348, RXJ 2129+00, ZWCL3146). Observations were taken using a 3 point position dither. The exposure time in each filter was 1170s so that the observations in the two filters was approximately one HST orbit per galaxy. Observations were taken between March 2008 and February 2009. The long pass filters, F125LP, F140LP, F150LP, and F165LP, have similar maximum wavelengths of 2000Å but minimum or cut-off wavelengths of 1250, 1370, 1470 and 1650Å respectively. The pixel scale for the SBC is approximately  $0''.034 \times 0''.030/\text{pixel}$ . The camera field of view is  $34''.6 \times 30''.8$ . These FUV observations are summarized in Table 1.

The ACS/SBC images were reduced with the ACS calibration pipeline producing calibrated drizzled images. Continuum images were shifted to the position of the line images and subtracted from the line images after multiplication by an adjusted corrective factor larger than 1 to take into account the additional continuum photons present in the line images. Our procedure was to increase the correction factor until regions of the image became negative. FUV and continuum subtracted Ly $\alpha$  images are shown in Figures 1-7.

### 2.2. Comparison images

Observed at the same time were optical images with the WFPC2 camera on board HST using the broad band F606W filter for Abell 1664, ZWCL 8193 and RXJ 2129.6+0005. Visible broad band images observed with WFPC2 were available from the Hubble Legacy Archive for the remaining galaxies in either the F702W filter (Abell 1835) or the F606W filter (ZWCL 348, ZWCL 3146, and Abell 11). The broad band optical images are shown for comparison in Figures 1-7.

We have overlaid  $3\mu\text{m}$  continuum observations as contours in Figures 1-7 on the FUV continuum images. These images were taken with the IRAC camera on the Spitzer Space Telescope and are described by Egami et al. (2006); Quillen et al. (2008). We find that the FUV and Ly $\alpha$  emission is located near the center of the brightest cluster galaxies as seen at  $3\mu\text{m}$ .

Chandra X-ray Telescope observations with the Advanced CCD Imaging Spectrometer (ACIS) were available from the archive for four of the galaxies; Abell 1664, Abell 1835, ZWCL 3146, and RXJ 2129+00. Exposure times are 11, 22, 49, and 12 ks respectively. The event files were binned to  $1''$  pixels and the resulting images smoothed with the *ciao* adaptive smoothing routine *csmooth* using the algorithm by Ebeling et al. (2006). Constant surface brightness X-ray contours are shown

for these four galaxies in Figures 2,3, 5 and 7 overlaid on the continuum subtracted Ly $\alpha$  images.

Figures 1-7 have been centered at the location of the central radio sources as measured from VLA archival data at 5 or 8.5 Ghz (with positions listed in Table 1). Coordinate errors measured from HST, Spitzer Space Telescope and ACIS Chandra X-ray Telescope observations are of order an arcsecond. The FUV and Ly $\alpha$  images lack contain point sources that could be used to register the images at sub-arcsecond scales.

### 2.3. Morphology

We find that all 7 galaxies observed display extended emission in both FUV continuum and Ly $\alpha$  emission. The FUV continuum is patchy, as was true for Abell 1795 and Abell 2197 (O’Dea et al. 2004). As discussed by (O’Dea et al. 2004) the FUV continuum is likely associated with young stars in star clusters. The Ly $\alpha$  morphology contains both clumps and a more diffuse or filamentary component. Diffuse or filamentary Ly $\alpha$  was also seen by O’Dea et al. (2004) in Abell 1795 and Abell 2597. The association between the Ly $\alpha$  and FUV continuum implies that the FUV continuum is responsible for the ionization of the Ly $\alpha$  emitting gas.

#### 2.3.1. Ly $\alpha$ and radio emission

Only two of the radio sources, those in RXJ 2129+00 and Abell 1835, were resolved in the VLA archival observations. For these two we have overlaid radio contours on the images showing Ly $\alpha$  emission so the orientation of the radio emission can be seen. In neither galaxy are the radio jets clearly associated with Ly $\alpha$  emission or lying near emitting filaments as was true for the nearer galaxies Abell 1795 and Abell 2597 (O’Dea et al. 2004). These two have redshifts of 0.6 and 0.8 whereas our nearest source has  $z = 0.15$ . The lack of any association between Ly $\alpha$  and radio emission in our sample may in part be due because the sources are more distant than the nearer two galaxies studied previously.

#### 2.3.2. Lopsidedness

All our BCGs display lopsidedness. Abell 11’s bright visible nucleus coincides with the brightest region of FUV continuum and Ly $\alpha$  emission. However this nuclear region is not centered on the outer isophotes as seen either in visible or  $3\mu\text{m}$  light (see Figure 1). The FUV and Ly $\alpha$  emission both show an additional emission region about  $2''$  west of the nucleus. For Abell 1664,  $3\mu\text{m}$  peak is located whether there are dust lanes in the visible band images implying that this is the galaxy nucleus. The outer  $3\mu\text{m}$  isophotes extend to the south-west where there is excess X-ray emission (see Figure 2). The lopsided X-ray morphology was also noted by Kirkpatrick et al. (2009). Abell 1835 also displays asymmetric X-ray contours. Its  $3\mu\text{m}$  contours are also not centered on the brightest regions seen the FUV, Ly $\alpha$  or visible band images (see Figure 3). For ZWCL 348 the visible and  $3\mu\text{m}$  emission peaks are nearly centered and the FUV emission peaks on the center of the galaxy. However the visible band image shows that the galaxy is disturbed and the outer contours seen in at  $3\mu\text{m}$  are not round (see Figure 4). The Ly $\alpha$  emission extends eastwards from the nucleus much further than to the west. Though the FUV

and  $L\alpha$  emission are centered on the  $3\mu\text{m}$  contours in ZWCL 3146, again the X-ray emission is lopsided, extending south-east of the nucleus (see Figure 5). For ZWCL 8193 there is a nuclear bulge visible in the visible and  $3\mu\text{m}$  images. However FUV and  $L\alpha$  emission is brighter north of the nucleus, and has a spiral shape suggesting that a smaller galaxy has been recently disrupted in the outskirts of the BCG (see Figure 6). RXJ 2129+00 also displays lopsided X-ray emission contours extending to the south-west. The  $L\alpha$  contours extend on only the northern-eastern side of the galaxy. The offset between radio and  $L\alpha$  peaks is small and so may be due to a registration error in the HST image (see Figure 7).

We find that most of these BCGs display strong asymmetries or uneven distributions in their star formation as seen from the FUV continuum images. In addition we have 4 galaxies with lopsided X-ray emission with Abell 1664 previously noted by Kirkpatrick et al. (2009). The offset of the BCG from the peak of the cluster X-ray emission is an indication of how close the cluster is to the dynamical equilibrium state, and decreases as the cluster evolves (Katayama et al. 2003). Loubser et al. (2009) found that BCGs tend to lie in cooling flows but found no correlation between the age of the BCG population and this offset, whereas Bildfell et al. (2008) found that blue BCGs tend to be within 10 kpc of the X-ray peak. The four galaxies we have with X-ray emission do have BCG within 10 kpc of the X-ray emission peak, consistent with the study by Bildfell et al. (2008) and are also located in cooling flows (O’Dea et al. 2008), consistent with the study by Loubser et al. (2009). Edwards et al. (2009) found that cooling flow BCGs often do not contain young populations, whereas O’Dea et al. (2008) found that estimated X-ray mass deposition rates are correlated with star formation rates.

For these galaxies,  $1''$  corresponds to 2–4 kpc (see Table 1) thus these asymmetries are on a scale of order 10–50 kpc. The high star formation rates of the galaxies studied here compared to others in the Rosat BCG sample may be related to the large scale X-ray structure. We will discuss this in more detail later.

### 2.3.3. Comparison to CO and $H\alpha$ observations

Emission from CO remained unresolved at a resolution  $6''$  for Abell 1835 and ZWCL 3146 (Edge & Frayer 2003). The nuclear  $24\mu\text{m}$  emission was unresolved (Quillen et al. 2008; Egami et al. 2006) for all of the BCGs studied here, though the nuclear region was red over a resolved region in the central few arc seconds in the mid-IR broad band images for Abell 1664 and ZWCL 8193 (Quillen et al. 2008). For comparison the point spread function FWHM for IRAC camera is  $1''.7$  at  $3\mu\text{m}$  (IRAC band 1) and  $2''.2$  at  $8\mu\text{m}$  (IRAC band 4) and  $7''$  at  $24\mu\text{m}$ . the two with the most extended FUV and  $L\alpha$  emission. Our UV observations have higher angular resolution than the CO or Spitzer observations but are consistent with the extent that these previous observations were able to resolve star formation regions. The star formation regions in these galaxies extend a few arcseconds corresponding to 5–10 kpc.

Abell 1664 has been observed using integral field spectroscopy by Wilman et al. (2006) in the  $H\alpha$  line. The continuum subtracted  $L\alpha$  emission images resembles the  $H\alpha$  image shown as Figure 2 by Wilman et al. (2006)

with a bright spot about  $2''$  from the nucleus to the south west. The bright spot we see just north of the nucleus does correspond to an  $H\alpha$  emission feature. However the  $L\alpha$  emission is brighter north west of the nucleus rather than north east of the nucleus as is true in  $H\alpha$ . It is likely that a more detailed comparison will reveal a large variation in  $L\alpha$  to  $H\alpha$  ratio suggesting either large variations in extinction or shock emission as photoionization models to predict a narrower range of intrinsic emission ratios (Ferland & Osterbrock 1985, 1986).

Wilman et al. (2006) also observed ZWCL 8193 and detected  $H\alpha$  emission at the galaxy center and in two clumps about  $3''$  north of the galaxy (see their Figure 17). Their  $H\alpha$  emission more closely resembles our FUV continuum image, though the  $H\alpha$  emission is stronger near the galaxy than north of the galaxy and we see stronger continuum emission north of the galaxy than near the galaxy center. Our  $L\alpha$  image shows diffuse emission over a region that is about twice the area than the  $H\alpha$  emission. The  $L\alpha$  emission exhibits a tail curving to the east from the north and almost looks like a spiral galaxy. The morphology suggests a gas rich galaxy has been disrupted and its remains are forming stars in the vicinity of the BCG.

### 2.4. Estimated Star Formation Rates

We use the FUV continuum flux to estimate star formation rates in these galaxies. The continuum flux was first corrected for Galactic extinction. Extinction correction was done using Galactic extinction at the position of each BCG and the extinction law by Cardelli et al. (1989) (as done in Table 5 by O’Dea et al. 2004 for Abell 1795 and Abell 2597). We then compared the count rate predicted for the observed filter by *synphot*<sup>1</sup> for a spectrum produced by STARBURST99<sup>2</sup> (Leitherer et al. 1999; Vazquez & Leitherer 2005). *synphot* is a general purpose package for synthetic photometry. Its utility for Hubble Space Telescope users arises from detailed models of HST instrument throughputs that are stored in the Calibration Data Base system.

The UV continuum estimated star formation rates are listed in Table 2. We compare the UV continuum estimated star formation with those based on the limited aperture  $H\alpha$  fluxes by Crawford et al. (1999) (using  $1''.3$  wide slit) or spectroscopic measurements from the Sloan Digital Sky Survey archive (using a  $3''$  diameter fiber) and those estimated from infrared observations with the Spitzer Space Telescope by Egami et al. (2006); Quillen et al. (2008); O’Dea et al. (2008). Neither the UV continuum estimated or  $H\alpha$  estimated star formation rates have been corrected for internal extinction. This Table also lists molecular gas masses by Edge (2001); Salome & Combes (2003).

Balmer decrements are available for most of the galaxies considered here and range from 3–5 (Crawford et al. 1999). The intrinsic optical extinction imply  $E(B-V) \sim 1$  and extinctions in the far UV of order 10. For an extinction this high we should not have detected any FUV continuum emission.

We note from table 2 that infrared star formation rates exceed those estimated in  $H\alpha$  and these exceed those es-

<sup>1</sup> [http://www.stsci.edu/hst/HST\\_overview/documents/synphot/hst\\_synphot1](http://www.stsci.edu/hst/HST_overview/documents/synphot/hst_synphot1)

<sup>2</sup> <http://www.stsci.edu/science/starburst99/>

timated from the FUV continuum. This would be consistent with patchy but significant levels of extinction. Large levels of extinction are also likely because of the high molecular gas content in these galaxies.

Previous comparisons between  $H\alpha$  and  $Ly\alpha$  flux suggested modest extinctions intrinsic to the cluster of order  $E(B-V) = 0.09-0.25$  (Hu 1992). This was done assuming an unabsorbed  $L\alpha/H\alpha$  ratio of 13 for photoionization and collision models (Ferland & Osterbrock 1986). However the BCGs considered by Hu (1992) were not chosen via their  $H\alpha$  luminosity. As  $H\alpha$  luminosity is correlated with both molecular gas mass and infrared luminosity (O’Dea et al. 2008) is it perhaps not surprising that the sample considered here would have higher estimated internal extinctions than the same considered by Hu (1992).

In short, FUV estimated star formation rates are about 10 times lower than those estimated from the Spitzer observations. Balmer decrements and molecular gas observations suggest that internal extinction could be extremely high in some regions. The discrepancy between the estimated star formation rates and the Balmer decrement suggest that internal extinction is patchy. As the infrared estimated star formation rate is least sensitive to extinction, it can be considered the most accurate, and suggests that about 90% of the FUV continuum has been absorbed.

O’Dea et al. (2008) noticed a discrepancy between the infrared estimated star formation rates and the size of the star forming regions. Here we have confirmed that the star forming regions are not large and remain under 20kpc. This puts the galaxies somewhat off the Kennicutt relation but (as shown by O’Dea et al. 2008 in their figure 8) but only by a modest factor of a few. While we confirm the discrepancy we find that it is not large enough that it could not be explained by other systematic effects such as an overestimate of the  $H_2$  mass. The CO to  $H_2$  conversion factor is suspected to be lower by a factor of a few (e.g., Israel et al. 2006) in galaxy centers compared to disk regions. If the same were true in these BCGs then they would like on the Kennicutt relation.

#### 2.4.1. $Ly\alpha$ emission

Table 3 must be discussed. xxx

### 3. DISCUSSION AND SUMMARY

In this paper we have presented high angular resolution images in FUV continuum and  $Ly\alpha$  of 7 brightest cluster galaxies that are actively forming stars. The emission in both continuum and  $Ly\alpha$  is resolved over a region 5-10 kpc large. Both continuum and line emission contains

clumps, but the  $Ly\alpha$  emission also contains a diffuse or filamentary component.

Star formation rates estimated from the FUV continuum are about 10 times lower than those estimated from the infrared, however, both the Balmer decrement in the central arcsec and detection of CO in these galaxies suggest that there are regions of high extinction. We suspect that a substantial fraction of the FUV emission is absorbed by internal extinction.

Comparisons between  $Ly\alpha$  and existing  $H\alpha$  images suggest that there are large variations in emission line ratio. This can be explained either by patchy extinction or with shocks, affecting the intrinsic line ratios.

Unlike Abell 1795 and Abell 2597 (O’Dea et al. 2004), we find no relation between the  $Ly\alpha$  morphology and the radio morphology in our galaxies. While both of these galaxies host star formation, it is at a lower level than estimated for the 7 of our sample. With the exception of Abell 1835 and RXJ 2129+00, the radio emission at 5 or 8 GHz (from archival VLA observations) is not resolved suggesting that these sources have fairly compact radio structures. This could be because nuclear fueling has been reduced by a previous AGN activity cycle and we are now seeing the galaxies following a period of relative quiescence. It is tempting to also account for the high star formation rate with a period of low feedback. Rapid cooling in the IGM fueling the current high star formation may be due to a previous reduction in energy deposited into the IGM.

We have also noted that most of our galaxies exhibit asymmetries in their distribution of star formation and 4 of them show lopsided X-ray contours. Feedback from an AGN (jets and bubbles) would not be expected to push the X-ray emitting gas off-center. However disturbances in the IGM could lead to higher cooling rates in the gas as the cluster relaxes and slowly evolves to equilibrium. Kirkpatrick et al. (2009) find that cooling rates could be high enough to fuel the star formation in Abell 1664. Similar cooling rates have been estimated for most of the other galaxies in our sample (O’Dea et al. 2008). If the high star formation rates are related to large disturbances in the IGM the radio quiescence of these sources requires another explanation. The large estimated molecular gas mass, Balmer decrements, discrepancies between star formation rates estimated in FUV continuum,  $H\alpha$ , and infrared imply that there is dense gas in these galaxies. We have resolved the regions of star formation and find that this dense gas is likely to be within the central 10-20 kpc. In this case radio jets could be frustrated as is thought to happen in CSS sources.

### REFERENCES

- Baum, S. A., Laor, A., O’Dea, C. P., Mack, J., & Koekemoer, A. M. 2005, *ApJ*, 632, 122  
Bildfell C., Hoekstra H., Babul A., Mahdavi A., 2008, *MNRAS*, 389, 1637  
Binette, L., Wang, J., Villar-Martin, M., Martin, P. G. & Magris, G. G. 1993, *ApJ*, 414, 535  
Cardelli, J. A., Clayton, G. C., & Mathis, J. S., 1989, *ApJ*, 345, 245  
Clampin, M., Sirianni, M., Hartig, G. F., Ford, H. C., Illingworth, G. D., Burmester, W., Koldewynd, W., Martel, A. R., Riess, A., Schrein, R. J., & Sullivan, P. C. 2004, *Scientific Detectors for Astronomy, The Beginning of a New Era*; eds. Amico, P., Beletic, J. W., & Beletic, J. E., p. 555-563, Kluwer Academic Publishers  
Crawford, C. S., Allen, S. W., Ebeling, H., Edge, A. C., & Fabian, A. C. 1999, *MNRAS*, 306, 857  
Donahue, M., Voit, G. M., O’Dea, C. P., Baum, S. A., & Sparks, W. B. 2005, *ApJ*, 630, L13  
Ebeling, H., Edge, A. C., Böhringer, H., Allen, S. W., Crawford, C. S., Fabian, A. C., Voges, W., & Huchra, J. P. 1998, *MNRAS*, 301, 881  
Ebeling, H., White, D. A., & Rangarajan, F. V. N. 2006, *MNRAS*, 368, 65  
Edge, A. C. 2001, *MNRAS*, 328, 762  
Edge, A. C., & Frayer, D. T. 2003, 594, L13  
Edwards, L. O. V., Robert, C., Molla, M., & McGee, S. L. 2009, *MNRAS*, 396, 1953  
Egami, E., et al. 2006, *ApJ*, 647, 922

- Egami, E., Rieke, G. H., Fadda, D., & Hines, D. C. 2006, ApJ, 652, L21
- Ferland, G. J., & Osterbrock, D. E. 1985, ApJ, 289, 105
- Ferland, G. J., & Osterbrock, D. E. 1985, ApJ, 300, 658
- Hu, E. M. 1992, ApJ, 391, 608
- Holtzman, J. A. et al. 1996, AJ, 112, 416
- Israel, F. P., Tilanus, R. P. J., & Baas, F. 2006, A&A, 445, 907
- Katayama H., Hayashida K., Takahara F., Fukita Y., 2003, ApJ, 585, 687
- Kirkpatrick, C. C., McNamara, B. R., Rafferty, D. A., Nulsen, P. E. J., Birzan, L., Kazemzadeh, F., Wise, M. W., Gitti, M., Cavagnolo, K. W. 2009, ApJ, 697, 867
- Leitherer, C. et al. 1999, ApJS, 123, 3
- Loubser, S. I., Sanchez-Blazquez, P., Sansom, A. E., & Soechting, I. K. 2009, MNRAS, 398, 133
- McNamara, B. R., Rafferty, D. A., Birzan, L.; Steiner, J.; Wise, M. W.; Nulsen, P. E. J., Carilli, C. L., Ryan, R., & Sharma, M. 2006, ApJ, 648, 164
- O'Dea, C. P., Baum, S. A., Mack, J., Koekemoer, A. M., & Laor, A. 2004, ApJ, 612, 1310
- O'Dea, C. P. et al. 2008, ApJ, 681, 10350
- Pipino, A., Kaviraj, S., Bildfell, C., Babul, A., Hoekstra, H., & Silk, J. 2009, MNRAS, 395, 462
- Quillen, A. C. et al. 2008, ApJS, 176, 39
- Rafferty, D. A., McNamara, B. R., & Nulsen, P. E. J. 2008, ApJ, 687, 899
- Salome, P., & Combes, F. 2003, A&A, 414, 657
- Vazquez, G. A., & Leitherer, C. 2005, ApJ, 621, 695
- Wilman, R. J., Edge, A. C. & Swinbank, A. M., 2009 MNRAS in press, arXiv:0902.4720
- Wilman, R. J., Edge, A. C., & Swinbank, A. M. 2006, MNRAS, 371, 93

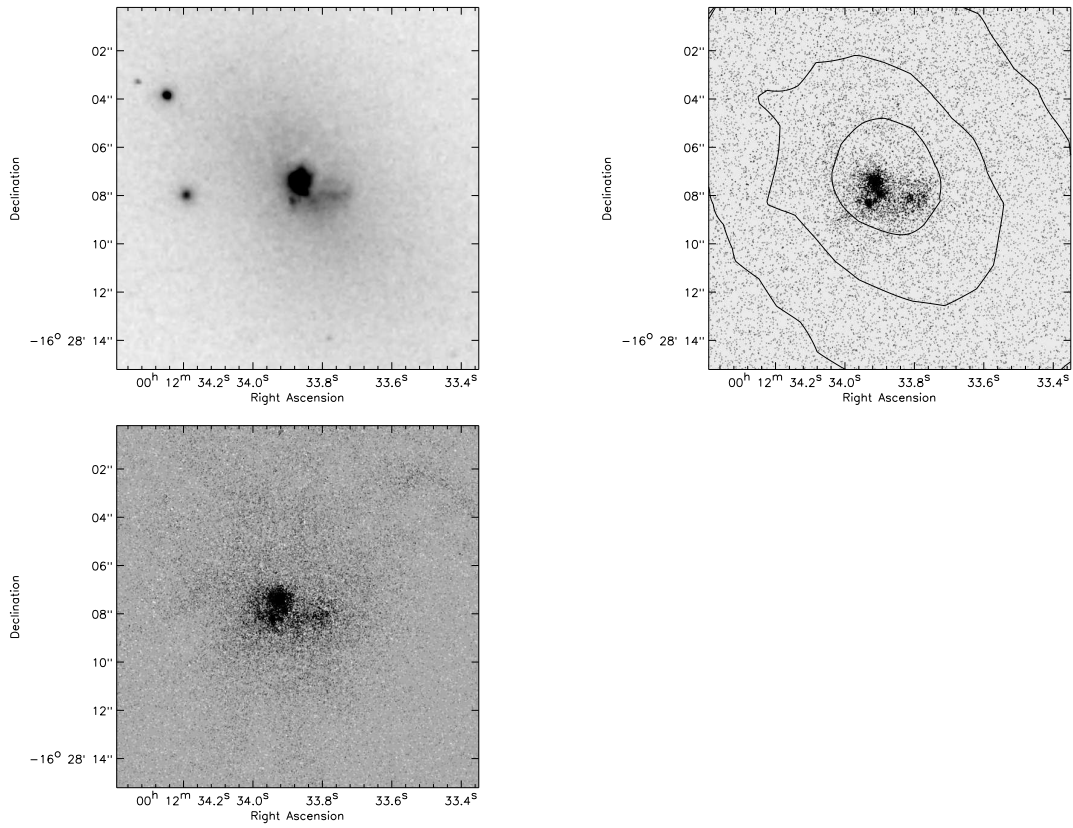


FIG. 1.— a) (upper left) Visible band HST image of Abell 11 in the F606W filter. b) (upper right) FUV continuum image. The FUV continuum image has  $3\mu\text{m}$  contours overlaid. Contour separation is a factor of two in surface brightness. The  $3\mu\text{m}$  image is a Spitzer IRAC band 1 image. c) (lower left) Continuum subtracted Ly $\alpha$  image.

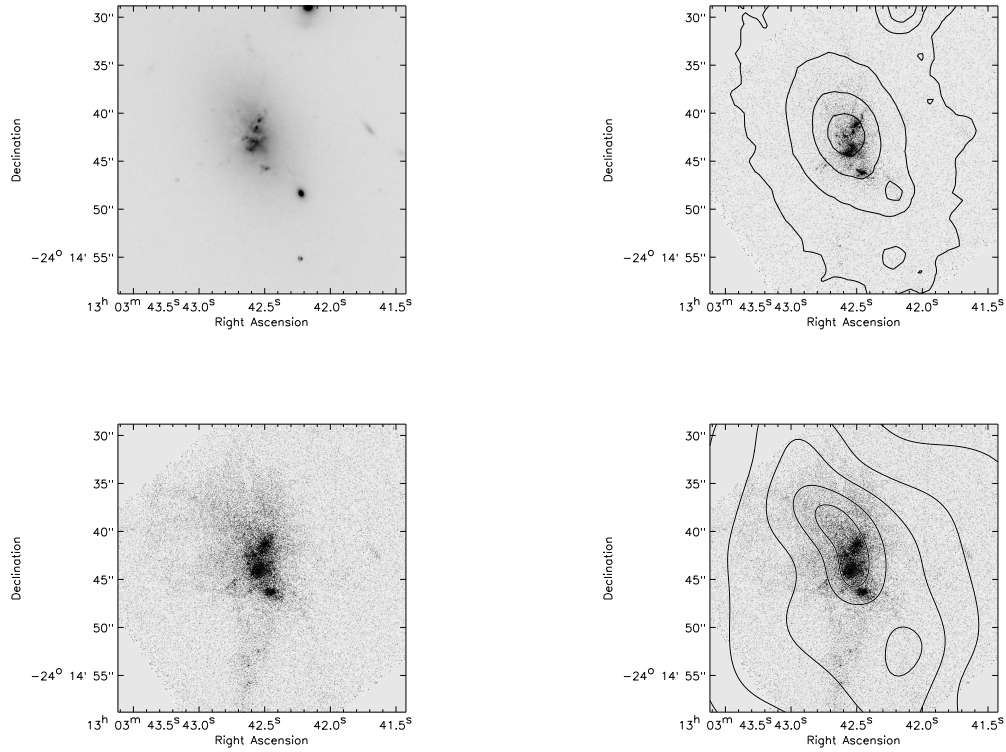


FIG. 2.— a) (upper left) Visible band HST image of Abell 1664 in the F606W filter. b) (upper right) FUV continuum image overlaid with  $3\mu\text{m}$  contours. c) (lower left) Continuum subtracted Lyman  $\alpha$  image of Abell 1664. d) (lower right) Continuum subtracted Ly $\alpha$  image with X-ray contours.

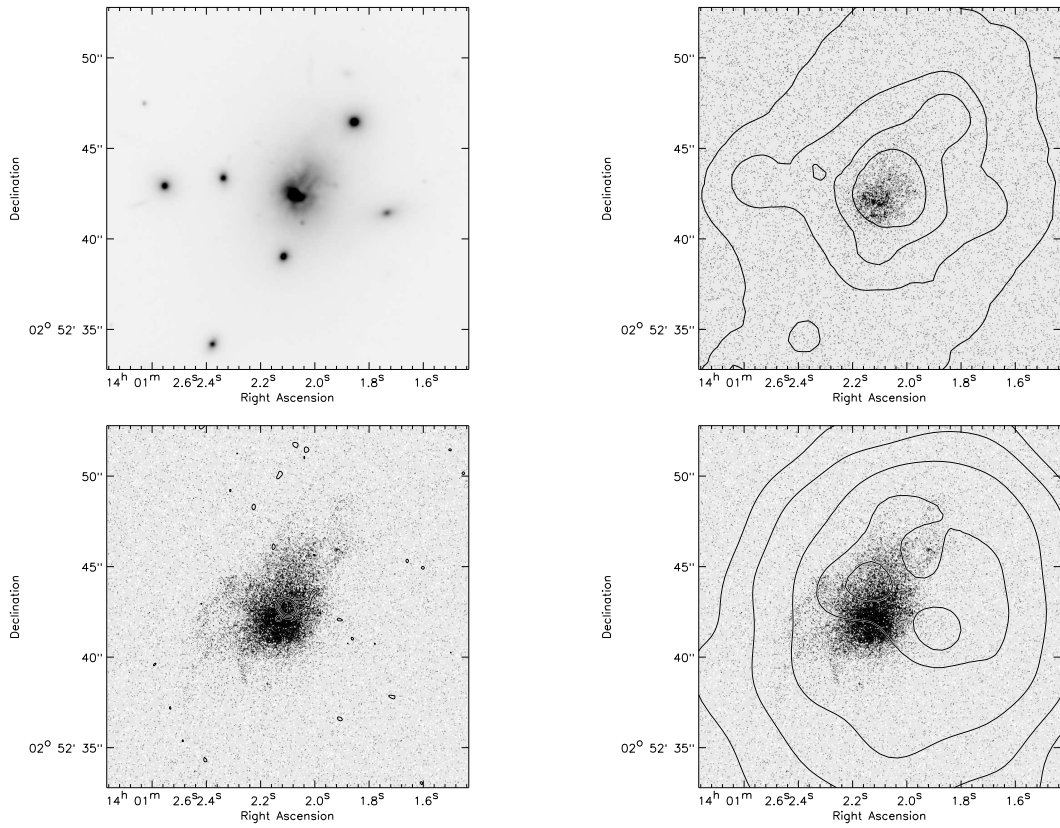


FIG. 3.— a) (upper left) Visible band HST image of Abell 1835 in the F702W filter. b) (upper right) FUV continuum image overlaid with  $3\mu\text{m}$  contours. c) (lower left) Continuum subtracted  $\text{Ly}\alpha$  image of Abell 1835 (grayscale) with 5GHz radio contours. d) (lower right) Continuum subtracted  $\text{Ly}\alpha$  image with X-ray contours.

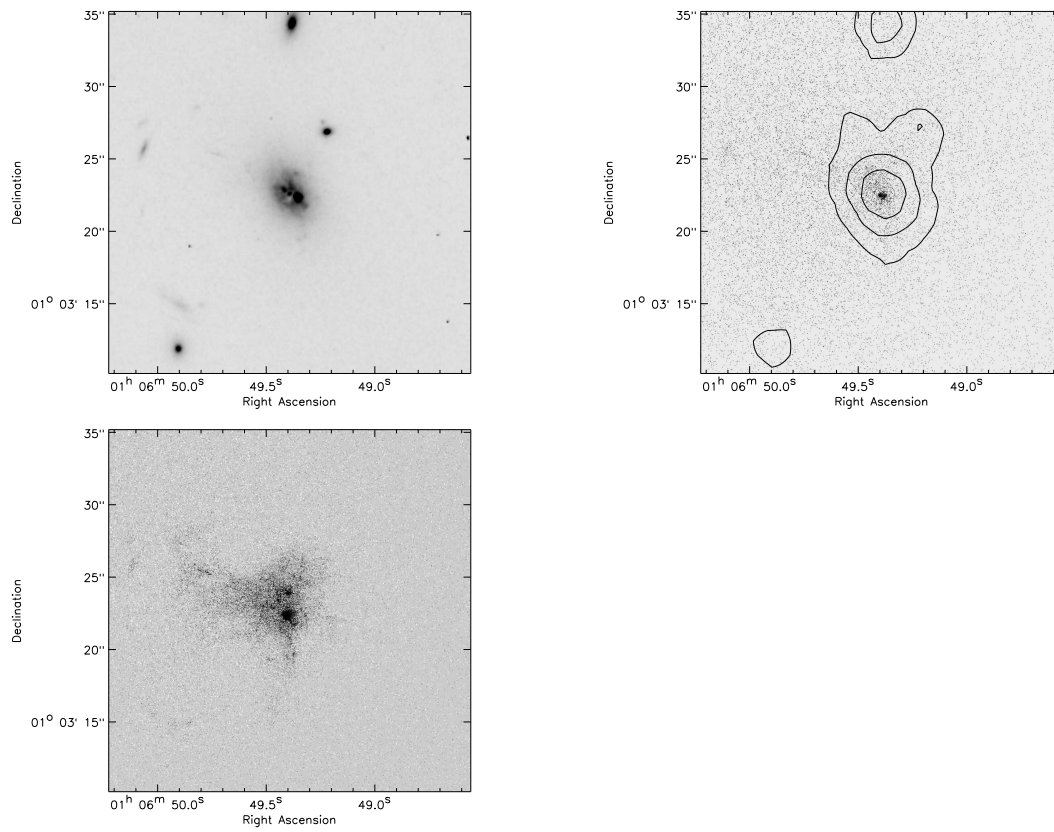


FIG. 4.— a) (upper left) Visible band HST image of ZWCL 348 in the F606W filter. b) (upper right) FUV continuum image overlaid with 3 $\mu$ m contours. c) (lower left) Continuum subtracted Lyman  $\alpha$  image of ZWCL 348.

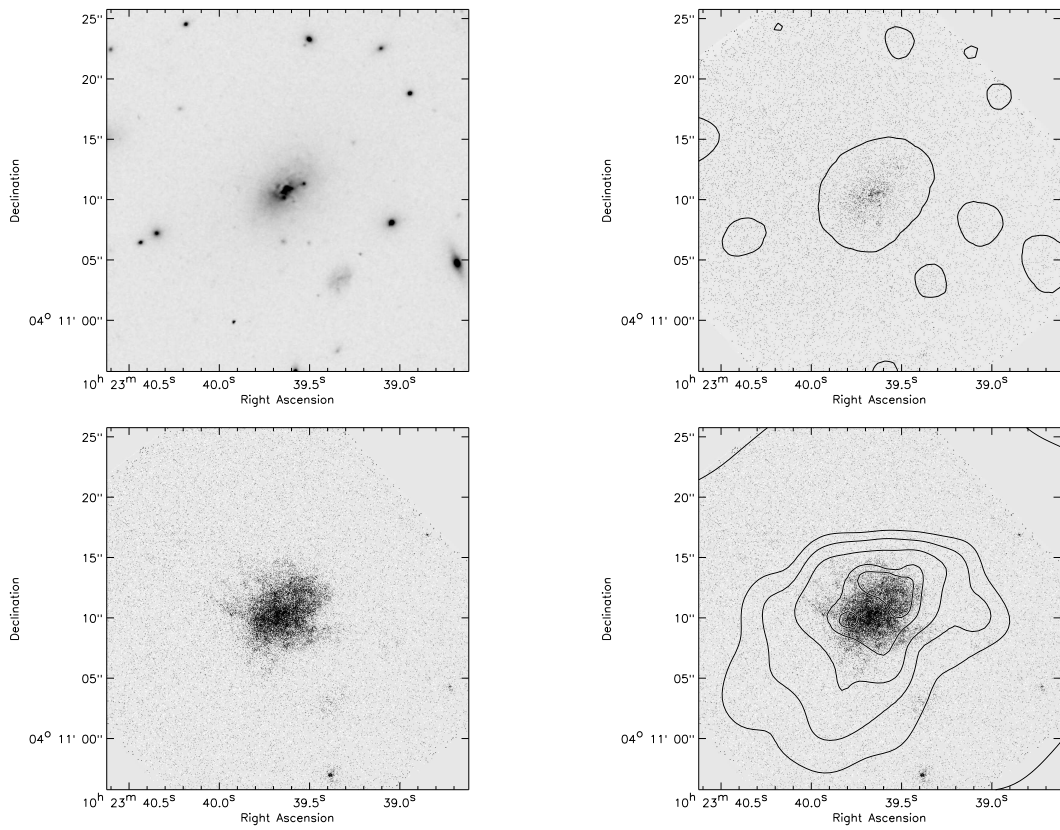


FIG. 5.— a) (upper left) Visible band HST image of ZWCL 3146 in the F606W filter. b) (upper right) FUV continuum image overlaid with  $3\mu\text{m}$  contours. c) (lower left) Continuum subtracted Lyman  $\alpha$  image of ZWCL 3146. d) (lower right) Continuum subtracted Lyman  $\alpha$  image with X-ray contours.

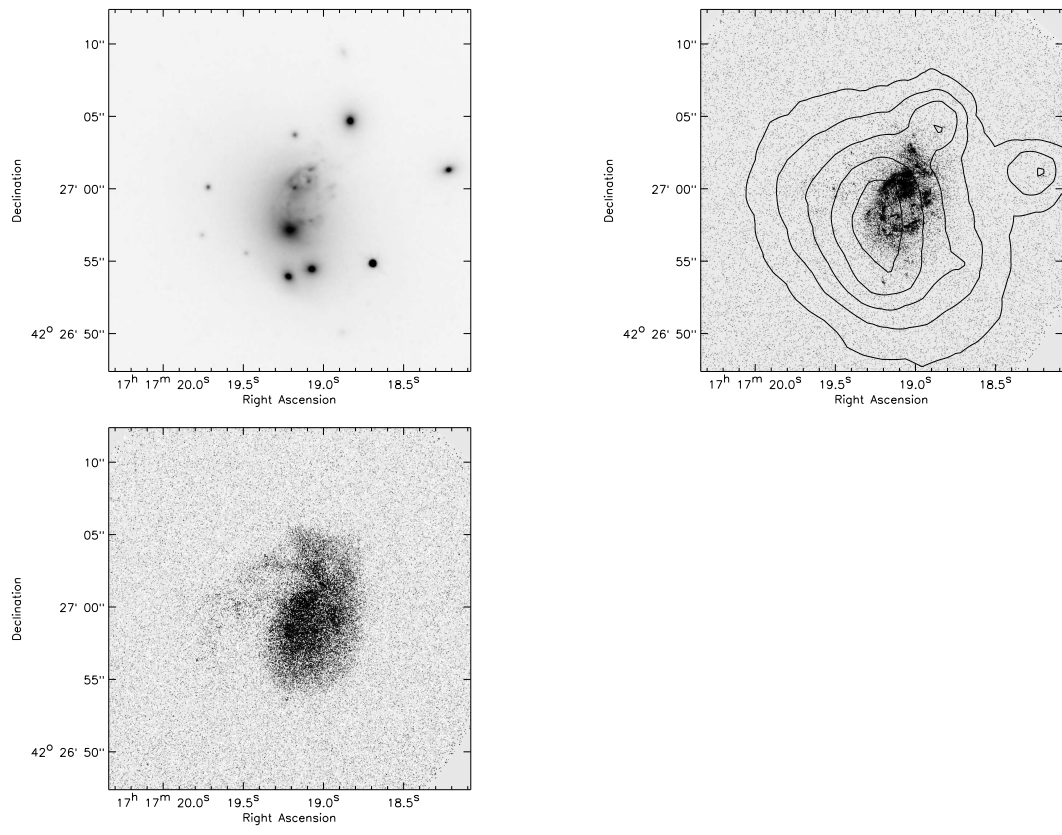


FIG. 6.— a) (upper left) Visible band HST image of ZWCL 8193 in the F606W filter. b) (upper right) FUV continuum image overlaid with 3 $\mu$ m contours. c) (lower left) Continuum subtracted Lyman  $\alpha$  image of ZWCL 8193.

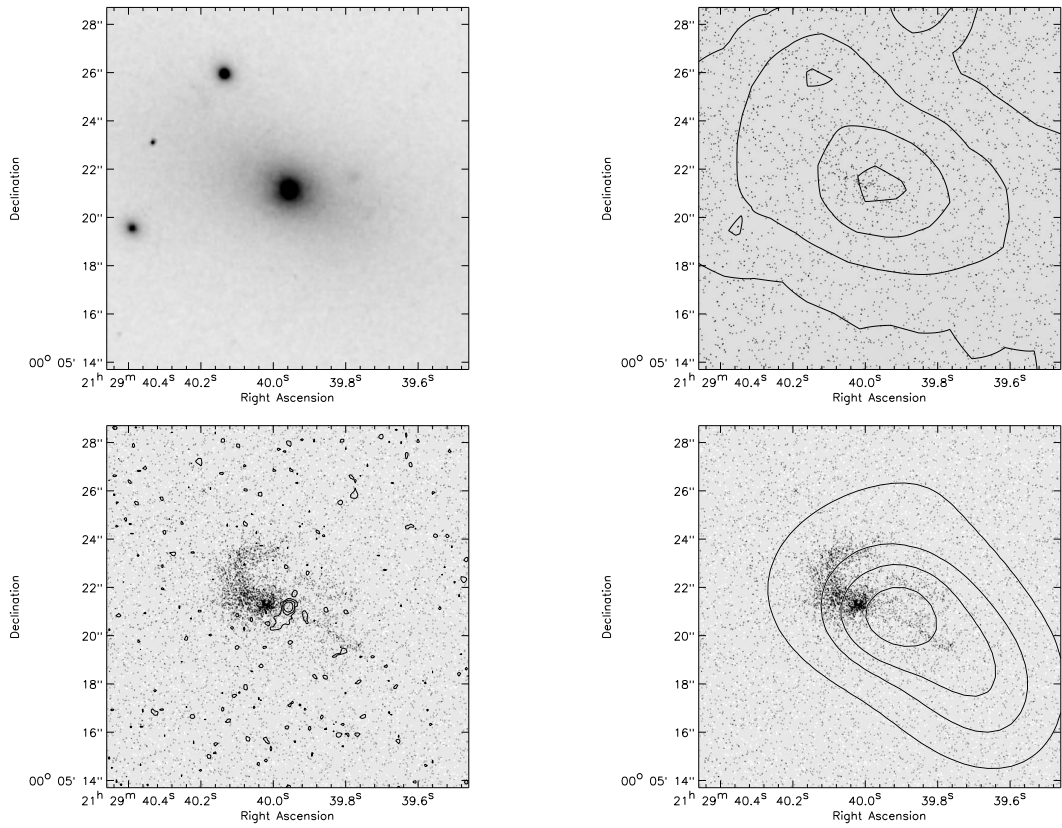


FIG. 7.— a) (upper left) Visible band HST image of RXJ 2129+00 in the F606W filter. b) (upper right) FUV continuum image overlaid with  $3\mu\text{m}$  contours. c) (lower left) Continuum subtracted Lyman  $\alpha$  image of RXJ 2129+00 overlaid with 8 GHz radio contours. d) (lower right) Continuum subtracted Lyman  $\alpha$  image with X-ray contours.